Study of Ge-rich GST device-dependent segregation aimed to the optimization of industrial grade embedded PCM

Petroni Elisa, M. Allegra, M. Baldo, L. Laurin, A. Serafini, L. Favennec, L. Desvoivres, J. Sandrini, C. Boccaccio, Yannick Le-Friec, et al.

Study of Ge-rich GST device-dependent segregation aimed to the optimization of industrial grade embedded PCM

E. Petroni[1], M. Allegra[1], M. Baldo[1], L. Laurin[1], A. Serafini[2], L. Favennec[3], L. Desvoivres[4], J. Sandrini[5], C. Boccaccio[5], Y. Le-Friec[3], A. Ostrovsky[3], P. Gouraud[3], A. Durel[3], R. Ranica[5], A. Redaelli[1]*

[1]Smart Power TR&D, STMicroelectronics, 20864 Agrate Brianza, Italy
[2]AGR FMT Physical Laboratory, STMicroelectronics, 20864 Agrate Brianza, Italy
[3]DIG FEM TR&D PDEV, STMicroelectronics, 38920 Crolles, France
[4]CEA-Leti, Univ. Grenoble Alpes, 38920 Crolles, France
[5]DIG FEM TR&D DNA, STMicroelectronics, 38920 Crolles, France

*Corresponding author: elisa.petroni@st.com

Key words: PCM, Ge-rich GST, EELS, compositional data analysis, statistics, reliability.

Ge-rich GST (GGST) alloys are the most promising materials for phase-change memory (PCM) in embedded applications, being able to fulfill the tough data retention requirements of automotive and consumer markets. GGST alloys are sensitive to thermal budgets and spatial confinement; thus, memory device process integration and architecture can strongly impact their final electrical properties and reliability. In this work, we will show how to monitor and control architecture, material and process-induced GGST modification, in order to exploit these modulations to meet the challenges of embedded technologies.

1. Introduction

In the embedded memory field of application, phase-change memories (PCM) are the most promising emerging technologies [1]. Thanks to their scalability and ease of integration in the back-end-of-line (BEOL), PCM are considered as valid replacement of classical flash-based approaches [1,2]. Nevertheless, conventional phase change material ($Ge_2Sb_2Te_5$) is not compatible with the high temperature data retention standard required by the automotive and consumer markets (years at 150 °C required from automotive and the 2 min at 260 °C from soldering reflow compliance as per JEDEC specifications) [1-3]. In fact, $Ge_2Sb_2Te_5$ has a low crystallization temperature, about 150 °C when measured with minute time-range ramps [1,4,5]. To overcome this limitation, Ge-rich GST (GGST) ternary alloys have been engineered, showing to meet markets' retention specifications due to their crystallization temperature above 350°C (ramp with minute time-range) [6,7], as demonstrated by P. Zuliani [3] and, more recently, by F. Arnaud [8,9] on 28nm FD-SOI platforms. In this framework, detailed characterization of GGST physical properties, especially once the chalcogenide is patterned and

fully integrated, has become a crucial need. In fact, being a strongly out-of-stoichiometry material, GGST is highly sensitive to thermal budget, experiencing different material features and electrical performance depending on its thermal history [10]. Previous literature has been focused on the characterization of the specific GGST crystallization kinetic, based on the decomposition in Ge and fcc-GST phases [13-18]. Indeed, this decomposition affects homogeneity of the material at the end of the process, resulting in a very resistive and dispersed electrical response [10-12]. In order to recover the resistance of the alloy to functional values for memory application, a forming step is required. The initiation of the material by applying a first firing pulse creates a compositionally uniform active area, which reduces median resistance value and dispersion of the cell distribution [11,12]. From an electrical point of view, this effect can be explained by an activation energy landscape model, where the forming step flattens the high-energy barriers of the conduction landscape, produced by the chemical decomposition of the alloy [11]. However, material decomposition also has an impact on electrical response and reliability after the forming step. In fact, the residual Ge decomposition and dissolution outside the active area is still influencing median resistance value and retention performance of SET and RESET states [10,12]. Thus, decomposition level and material homogeneity at the end of the process have a huge impact on the final electrical performance of the memory cell. However, a detailed study of the crystallization and decomposition mechanisms of GGST as a function of process integration parameters, i.e., device architecture, alloy composition and integration of BEOL materials, is still lacking. Previous works have partially covered this gap by studying the segregation and crystallization of GGST in function of a realistic sequence of thermal budgets, i.e., in function of BEOL process integration [19,20]. To achieve this goal, a new statistical methodology of chemical STEM-EELS (Electron Energy Loss Spectroscopy in Scanning Transmission Electron Microscopy mode) mapping post-elaboration has been introduced, capable of dealing with composite materials with highly inhomogeneous composition. This new methodology has been demonstrated to properly consider compositional dispersion and to assess segregation and clustering of the material through new metrics for elemental evaluation [20].

In this work, exploiting the metrics of the statistical methodology already developed, an extended test case, that includes device architecture trials and material composition tuning, is presented. The goal is to study GGST segregation mechanism in function of all the possible process parameters, in order to achieve a complete description of the chalcogenide physical mechanisms, once patterned and fully integrated in an industrially targeted device.

2. Experimental Section

GGST alloy samples were extensively characterized by STEM techniques conducted on electron-transparent lamellae obtained by focused ion beam (FIB). The evolution of the alloy microstructure was observed by dark-field STEM micrographs (DF-STEM), while high spatial resolution chemical analyses were carried out by EELS. The lamellae were obtained using a Thermofischer Helios G5UX FIB. Low energy milling was used during the final thinning steps to limit heating and ballistic effects of ion irradiation on GGST film. The STEM images were performed with a Thermofischer Themis Z G3 aberration-corrected scanning transmission electron microscope equipped with an electron gun monochromator operating at 200 kV acceleration voltage. To minimize the electron beam damage and effects on the crystallization process, all the STEM images and EELS maps were acquired with a low beam current (0.5 nA). The EELS measures were carried out at 1 eV/channel energy resolution with the post column Quantum Gatan Imaging Filter. The GGST elemental maps were acquired with a step size of 0.8 nm and the Gatan ® GMS Digital Micrograph 3.23 software was employed for the data elaboration.

Selected vehicle for our experiment is integrated PCM cells in Wall [3,5] and "Fully confined" (see Results section) architectures in 28nm technology [8,9]. Material analysis has been performed on pristine material before programming. The integrated PCM stack is composed of a tiny under-layer (UL) of $Ge_2Sb_2Te_5$, with thickness equal to 10% of the total one, and another layer of Ge-rich GST alloy, with different compositions. In particular, the GGST alloy has been optimized to fulfill automotive requirements, with a crystallization temperature of about 370°C (ramp rate 10°C/min) [3]. From now on we will refer to the integrated PCM stack by simply naming the Ge-rich GST layer.

3. Statistical methodology overview

As stated in the "Introduction", the analysis of the present test case will be performed by applying the previously reported statistical methodology [20]. The core idea of the method is to quantify the dispersion of the compositional distribution obtained from the composite GGST samples, corresponding to its degree of segregation and crystallization [20]. In **Figure 1**, three different BEOL-ended GGST devices in Wall architecture, differing for the level of process optimization (from BEOL1 to BEOL3 dielectric deposition has been modified reducing the overall amount of thermal budget), are shown. From the DF-STEM images in the first line of Figure 1, it is observed that the degree of crystallization is gradually modulated in the three samples, passing from a coarser grain texture in BEOL1 to a finer one in BEOL3. This observation is in line with the chemical analysis, reported in the second line of Figure 1 as EELS maps of overlapped Ge, Sb and Te signals coded with a RGB color scale (i.e., red corresponds

to Ge, green to Sb and blue to Te). From BEOL1 to BEOL3, the degree of chemical segregation decreases according to the corresponding crystallinity level, eventually returning smaller and less bright red or blue areas in BEOL3 map (corresponding to Ge-rich and Te-rich clusters).

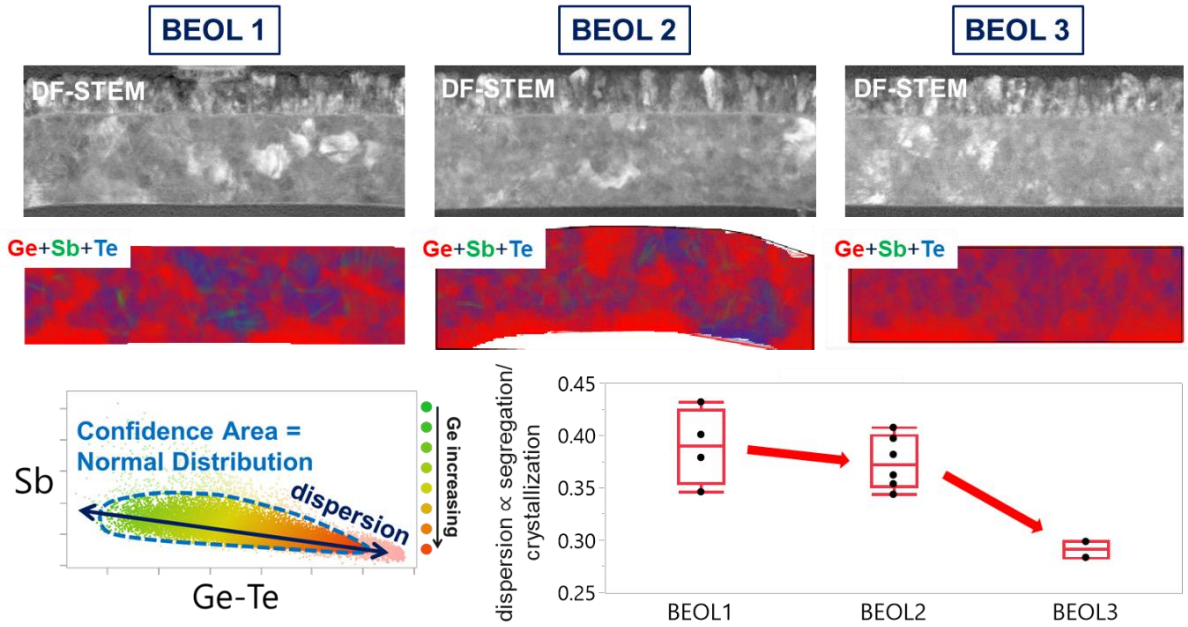

Figure 1. Physical and chemical analysis of 3 different BEOL: in the first line DF-STEM images of GGST-based devices in Wall architecture are reported; in the second line EELS maps of Ge, Sb and Te signals superposition coded with RGB color scale are shown; in the third line on the left an illustrative scatter plot of Sb vs. Ge-Te for BEOL1 sample is shown, with arrow indicating the dispersion proportional to the degree of material crystallization and segregation; in the third line on the right the results of statistical methodology for the 3 different BEOL are reported, where effective metric for segregation and crystallization of Ge/fcc-GST is highlighted.

The level of material evolution, qualitatively described by the DF and EELS images, is also well reported by the Sb vs. Ge-Te scatter plots, where each point in the plot corresponds to a pixel in the EELS map. An illustrative scatter plot is reported in the third line of Figure 1 on the left for the BEOL1 sample. As shown in the image, the point distribution is preferentially spread along a specific direction of the scattering space, roughly corresponding to that of the Ge-Te. The physical meaning of such directional dispersion is linked to the nature of segregation in the GGST, and the features of the TEM technique used for this analysis. Considering that the Ge-rich compositions crystallize due to the decomposition of the Ge and fcc-GST phases [14,17], we should observe two well-defined, i.e., not-spread and Gaussian, distributions in the scatter plot belonging to the decomposed compositions. However, because the TEM integrates the

EELS chemical signals over the entire thickness of the lamella, the scatter plot shows all the compositions found between the two segregated phases, mainly along the Ge-Te direction, due to the overlapping of different fcc-GST and Ge grains in the sample thickness. Thus, the dispersion of the obtained chemical distribution along this specific direction corresponds to the level of GGST segregation into the two sub-phases of the material, and it could be considered as an effective metric for the evaluation of its degree of crystallization and segregation [20]. To quantify this elongation, the individuation of the intrinsic part of distribution, more Gaussian-like, is needed [21,22]. The calculation of Mahalanobis distance for the screening of the outlier population [22,23] allows to isolate the normal distribution through an ellipse at 90% of confidence (see third line of Figure 1 on the left). From the normal population, it is very easy to extract the main dispersions of the distribution on the corresponding principal components [23]. The one along the Ge-Te direction, as reported in the scatter plot of Figure 1, is directly proportional to the degree of segregation and crystallization of the material, giving us a quantitative metric to evaluate by-process segregation [20]. The results of such elaboration are reported in the third line of Figure 1 on the right for the three BEOL-ended GGST. According to the graphical description discussed above, the metric is capable to track and quantify the modulation of crystallization and segregation passing from BEOL1 to BEOL3.

4. Experimental results

In this section, the analysis through the statistical methodology on the extended test case, including different device architectures and material compositions, is presented.

In **Figure 2**, physical and chemical analysis of GGST integrated with BEOL1 in two different architectures is reported (see first and second line of Figure 2), together with a schematic of the corresponding devices (see third line of Figure 2). Differently from Wall architecture, where a strip of chalcogenide material (in orange in the third line of Figure 2) lays on top of many heater elements (in yellow in the third line of Figure 2), which individuate the position of the single memory cell [3,5], in the Fully confined architecture GGST cubic structures with square base of 1000 nm^2 order of magnitude singularly land on top of the thin heater elements. Just by graphically inspecting the first two lines of Figure 2, which report DF-STEM images and EELS chemical maps, respectively, it is very difficult to compare the segregation and crystallization levels of the two architectures. In contrast to the case presented previously, graphical inspection does not even return basic observations. For this reason, the application of statistical methodology gains even more importance, enabling comparison even in cases where qualitative image and map analysis is not sufficient.

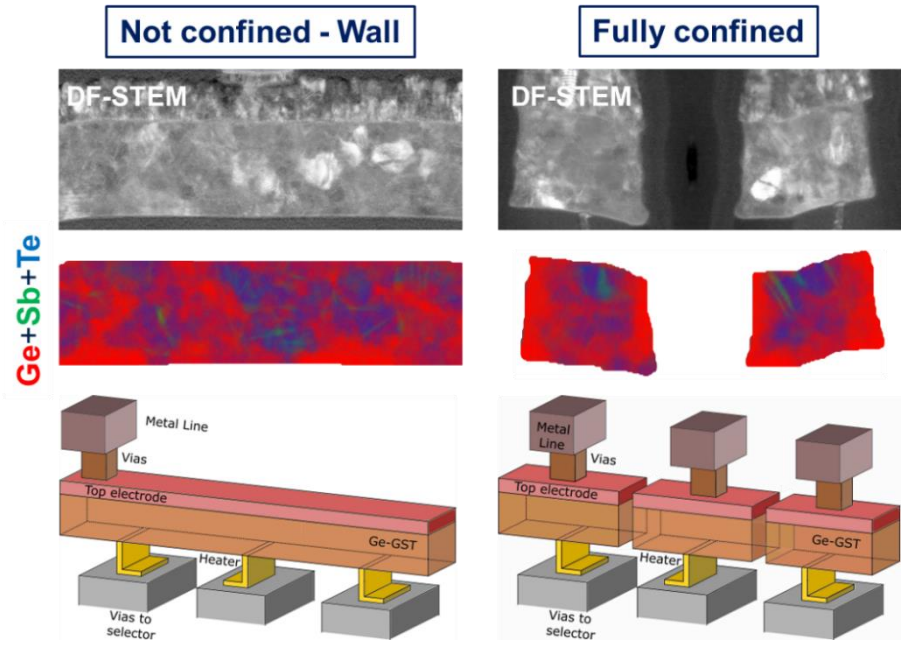

Figure 2. Physical and chemical analysis of Wall and Fully confined architectures integrated with BEOL1: in the first line DF-STEM images of GGST-based devices are reported; in the second line EELS maps of Ge, Sb and Te signals superposition coded with RGB color scale are shown; in the third line schematics of the two architectures are shown.

In **Figure 3a**, the results of the statistical methodology applied on samples of Figure 2 are shown. Both scatter plots (on the bottom of Figure 3a) and effective metrics (on the top of Figure 3a) show an increased level of segregation in the Fully confined case. This result is explained by the crystallization kinetic of patterned GGST, where the dominant process is the heterogeneous nucleation from the interfaces of the device [14]. This mechanism is shown in **Figure 3b**, where a partially crystallized GGST in Wall architecture is physically analyzed in the perpendicular direction to the chalcogenide strip (see Wall architecture schematic in Figure 2). As highlighted in the top image of Figure 3b with the dashed line, crystallization starts from the bottom and lateral interfaces of the material. From the chemical point of view (see bottom EELS map of Figure 3b), Ge segregation appears at the crystallization front (see arrows in the EELS map), according to the description of the phenomenon given in the literature [13-15]. Thus, having increased the number of available interfaces for heterogeneous nucleation in the Fully confined structure, faster crystallization kinetics can be assumed. As a consequence, for the same amount of thermal budget (i.e., same BEOL1) the Fully confined architecture experiences stronger segregation at the end of the process.

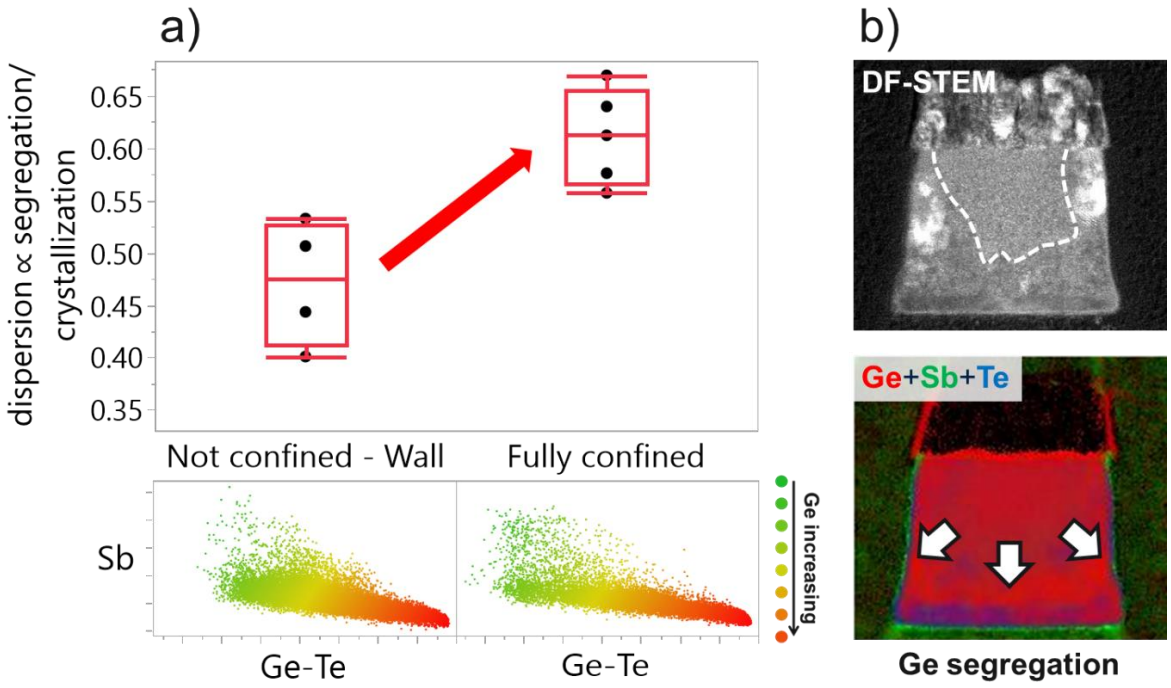

Figure 3. Results of statistical methodology on Wall and Fully confined architectures: a) on the top effective metric for segregation and crystallization of GGST in the two architectures is reported, on the bottom corresponding Sb vs. Ge-Te scatter plot are shown; b) DF-STEM and EELS analysis for a partially crystallized GGST in Wall architecture, perpendicularly to chalcogenide strip direction. Dashed line indicates crystallization front and arrows highlight Ge segregation.

With this result, we have also demonstrated the potential of this methodology in the evaluation of GGST segregation in different architectures.

A similar analysis can also be performed for different alloy compositions with the same architecture, in this case a Fully confined structure. The choice of the Fully confined architecture was dictated by the higher segregation found previously, which should maximize the possible differences between the two compositions at the end of the process.

Figure 4 shows the two compositions chosen for the analysis according to their main characterizing properties: Ge amount and crystallization temperature. In fact, by increasing Ge from $Ge_2Sb_2Te_5$ along the pseudo-binary line reported in green in the ternary diagram (see Figure 4a), it is possible to increase the crystallization temperature of the corresponding alloy to 350°C and above (see Figure 4b, here measured with a ramp rate of 10°C/min) [6]. Specifically, in Figure 4b, the two dashed lines are indicating the chosen compositions: the GGST one, optimized to have a temperature of about 370 °C (see Experimental Section) [2,3], reported in purple; and the γGST, characterized by a smaller amount of Ge and a lower crystallization temperature (of about 250 °C, measured with minute time-range ramp), reported

in magenta. The choice of γGST, which is characterized by a reduced amount of Ge, is aimed at verifying a possible mitigation of material segregation at the end of the same integration process, i.e., BEOL1. In fact, the lower the amount of Ge, the weaker the propensity of the Ge-rich alloy to decompose [17,18].

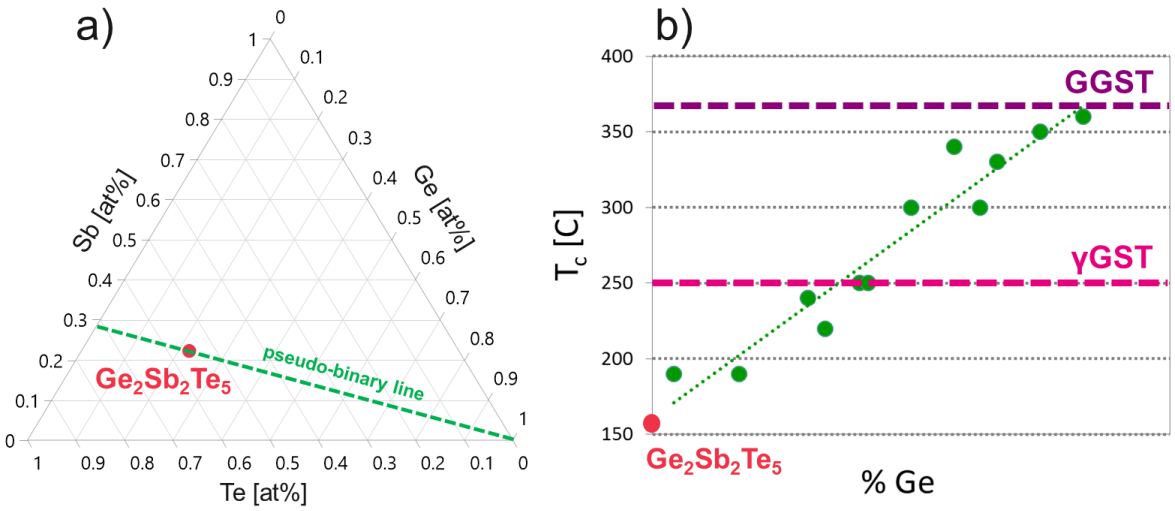

Figure 4. Exploration of Ge-rich corner of Ge-Sb-Te ternary diagram: a) specific pseudo-binary line explored by increasing Ge amount from $Ge_2Sb_2Te_5$; b) measured crystallization temperatures (ramp rate 10°C/min) along pseudo-binary line. The two dashed lines indicate the chosen compositions for the study, GGST and γGST reported in purple and magenta, respectively.

In **Figure 5**, complete characterization and statistical analysis of both GGST and γGST are reported. By graphically comparing the physical characterization results of the two selected compositions (first two columns of Figure 5), it is observed that γGST has a coarser grain texture than GGST and wider Ge- and Te-rich areas. In this case, it is difficult to rely on these qualitative observations, because the two alloys have a completely different composition, thus probably different crystallization kinetics (i.e., different grain sizes) [14,17] and different center-points for the chemical data (i.e., different colorations and sizes for Ge- and Te-rich areas). However, the statistical methodology takes into account the value of the center-points of the chemical distributions (see third column of Figure 5), normalizing the metrics to the actual composition of the material [20]. Therefore, this analysis procedure allows us to compare the level of chemical segregation in the two cases. The obtained results are reported in the fourth column of Figure 5: γGST shows slightly more segregation than GGST, probably because, although it has less Ge, the thermal budgets of BEOL1 are more impactful due to its lower crystallization temperature (of about 250 °C), accelerating the evolution process [18].

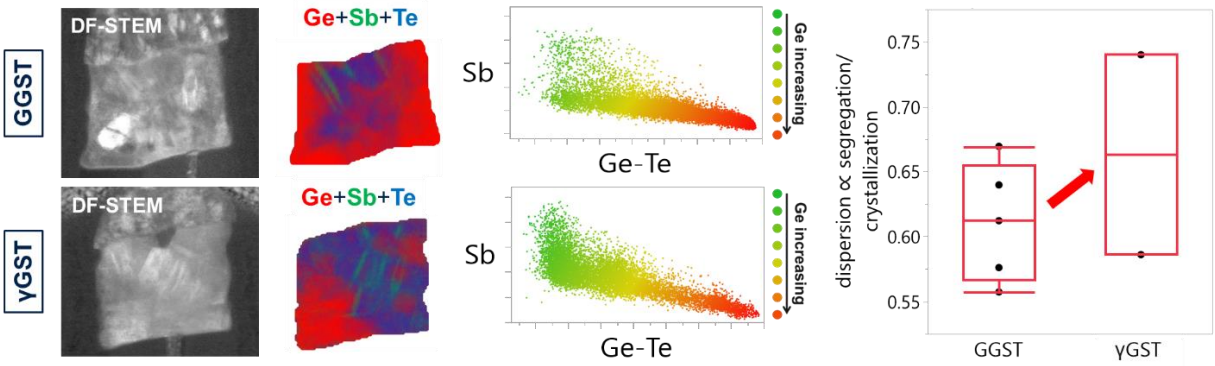

Figure 5. Physical characterization and statistical analysis for GGST and γGST in Fully confined architecture: in the first and second columns DF-STEM images and EELS maps coded with RGB color scale are reported; in the third column Sb vs. Ge-Te scatter plots are shown; in the fourth column effective metric for segregation and crystallization of GGST and γGST is reported.

5. Discussion

Figure 6 shows a summary of the statistical metrics extracted from the test cases displayed from Figure 1 to Figure 5. The linear modulation of segregation as a function of the different trials explored (BEOL, architecture and composition) can be identified from the graph on the top. Thus, assuming a pseudo-linear trend of the metric as a function of the tested variables:

$$Dispersion \propto segregation \sim a \cdot BEOL + b \cdot architecture + c \cdot composition, \quad (1)$$

it might be interesting to investigate how much the individual variables weigh on the amount of final segregation. A fitting model can then be applied according to the law given in (1), eventually returning an estimation of the variable's weight on the assumed trend [23,24]. It is worth mentioning that the variables considered are categoric, so the actual implementation of the fitting model requires a variable management step to apply a pseudo-linear trend [23]. The graph on the bottom of Figure 6 shows the results of the fitting displayed by individual variables. The dashed red lines indicate the conditions of the variables for the reported curves. Only one condition is shown in the graph because no inversion or distortion of trends has been observed by varying variables' choice for center-point [23,24]. The error bars are reported in blue, while the background color highlights the resulting variable's weight on the linear trend. Looking at the steepness of the curves, it is evident that the segregation is most primarily modulated by BEOL and architecture, with the latter being the most influencing factor (see the background colors). On the other hand, the composition variable seems to have less impact on the assumed modulation, as shown in the graph by its low linear coefficient [24]. Therefore, we can conclude that the main factors impacting segregation in this experiment are related to the

device process (i.e., BEOL and architecture) and that careful optimization of its characteristics is mandatory. We already know that process integration features can impact the final performance of memory cells, tuning the segregation level of the material and eventually its programming features [10].

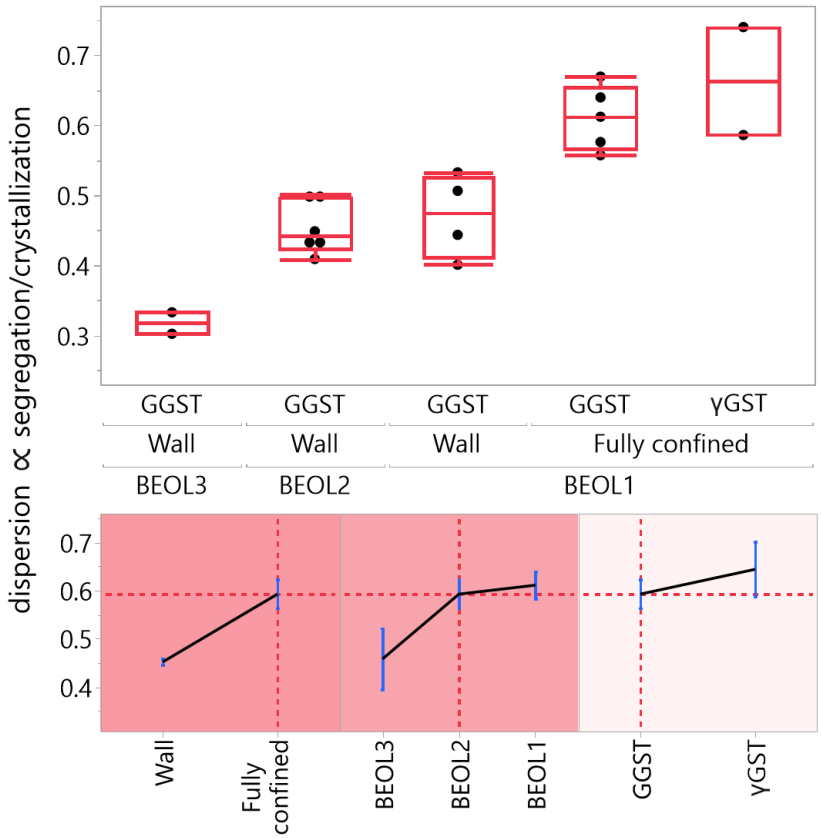

Figure 6. Summary of the effective metrics extracted from BEOL, architecture and composition trials and related fit results: on the top effective metric for segregation and crystallization in function of BEOL, architecture and composition; on the bottom results of the fitting of effective metric displayed by single variable.

From the point of view of the out-of-fab material segregation reported in this analysis, adjusting material composition to mitigate alloy inhomogeneity at the end of the process is not totally resolving, because of the compensation effect between the lower Ge content (i.e., the lower segregation propensity [17]) and lower crystallization temperature (see Figure 4b). Moreover, reducing the Ge amount in the material will have an impact on the electrical behavior of the device after program, also reducing its retention capability [3]. Thus, a higher Ge content is suggested for automotive and consumer applications, e.g., according to the GGST sample. In this view, fine optimization of process integration and device characteristics has been demonstrated to be the strongest players in improving the quality of out-of-fab material, i.e.,

degree of segregation and crystallization, thus improving the device electrical performance [10,20].

6. Conclusion

In this work, an extended test case of device-dependent segregation of Ge-rich GST alloys has been evaluated through the application of a statistical method [20]. Device architecture and material composition have been explored as possible modulating factors of material segregation. A Fully confined architecture has been compared with a more standard one, namely the Wall architecture, showing a higher level of crystallization and segregation due to the presence of multiple heterogeneous nucleation interfaces [14]. Then, two Ge-rich GST alloys have been analyzed, which returned a similar level of segregation due to the balance between the Ge amount in the alloy and the sensitivity to thermal budgets [17,18]. In conclusion, a fitting on segregation level has been performed, in function of all the already known sources of material inhomogeneity (BEOL, architecture and composition), revealing the main players in the segregation evolution of Ge-rich GST alloys at the industrial level [23,24]. BEOL and architecture have been proved to be the main modulating factors of segregation, which is an already well-known parameter for regulating cell reliability []. Thus, considering the weakness of less Ge-rich alloys about retention performance [3], this work highlights the need to carefully tune process integration and device characteristics to optimize the final electrical performance of appropriately Ge-rich GST-based embedded PCMs [10,20].

Acknowledgements

The authors would like to thank Philippe Brun, Marc Guillermet, Catherine Châton (CEA-Leti, Crolles), Jérôme Dubois, Xavier Gérard, Sarah Lamy, Julie Poulet, Sarah Rubeck, Claudette Mansour, Jean-Christophe Grenier, Marion Croisy, Délia Ristoiu (STMicroelectronics, Crolles) and all the colleagues of the ePCM Competence Center and the AGR FMT Physical Laboratory (STMicroelectronics, Agrate Brianza) for the support in device fabrication, data acquisition, elaboration and for the fruitful discussions.

Received: ((will be filled in by the editorial staff))
Revised: ((will be filled in by the editorial staff))
Published online: ((will be filled in by the editorial staff))

References

[1] P. Cappelletti, R. Annunziata, F. Arnaud, F. Disegni, A. Maurelli, P. Zuliani, *J. Phys. D: Appl. Phys.* **2020**, 53, 193002.

[2] R. Annunziata, P. Zuliani, M. Borghi, G. De Sandre, L. Scotti, C. Prelini, M. Tosi, I. Tortorelli, F. Pellizzer, *2009 IEEE International Electron Devices Meeting* **2009**, pp. 1-4.

[3] P. Zuliani, E. Varesi, E. Palumbo, M. Borghi, I. Tortorelli, D. Erbetta, G. Dalla Libera, N. Pessina, A. Gandolfo, C. Prelini, L. Ravazzi, R. Annunziata, *2013 IEEE Transactions on Electron Devices* **2013**, 60, pp. 4020-4026.

[4] F. Pellizzer, A. Benvenuti, B. Gleixner, Y. Kim, B. Johnson, M. Magistretti, T. Marangon, A. Pirovano, R. Bez, G. Atwood, in *Proceedings of the 2006 Symposium on VLSI Technology*, Honolulu, HI, USA, June **2006**, pp. 122-123.

[5] P. Fantini, *J. Phys. D: Appl. Phys.* **2020**, 53, 283002.

[6] H. Y. Cheng, T. Hsu, S. Raoux, J.Y. Wu, P. Du, M. Breitwisch, Y. Zhu, E. Lai, E. Joseph, S. Mittal, R. Cheek, A. Schrott, S. Lai, H. Lung, C. Lam, *2011 International Electron Devices Meeting* **2011**, pp. 3.4.1-3.4.4.

[7] A. Redaelli, E. Petroni, R. Annunziata, *Materials Science in Semiconductor Processing* **2022**, 137, 106184.

[8] F. Arnaud, P. Zuliani, J. Reynard, A. Gandolfo, F. Disegni, P. Mattavelli, E. Gomiero, G. Samanni, C. Jahan, R. Berthelon, O. Weber, E. Richard, V. Barral, A. Villaret, S. Kohler, J. Grenier, R. Ranica, C. Gallon, A. Souhaite, D. Ristoiu, L. Favennec, V. Caubet, S. DelMedico, N. Cherault, R. Beneyton, S. Chouteau, P. Sassoulas, A. Vernhet, Y. Le Friec, F. Domengie, L. Scotti, D. Pacelli, J. Ogier, F. Boucard, S. Lagrasta, D. Benoit, L. Clément, P. Boivin, P. Ferreira, R. Annunziata, P. Cappelletti, *2018 IEEE International Electron Devices Meeting* **2018**, pp. 18.4.1-18.4.4.

[9] F. Arnaud, P. Ferreira, F. Piazza, A. Gandolfo, P. Zuliani, P. Mattavelli, E. Gomiero, G. Samanni, J. Jasse, C. Jahan, J. P. Reynard, R. Berthelon, O. Weber, A. Villaret, B. Dumont, J. C. Grenier, R. Ranica, C. Gallon, C. Boccaccio, A. Souhaite, L. Desvoivres, D. Ristoiu, L. Favennec, V. Caubet, S. Delmedico, N. Cherault, R. Beneyton, S. Chouteau, P. O. Sassoulas,

L. Clement, P. Boivin, D. Turgis, F. Disegni, J. L. Ogier, X. Federspiel, O. Kermarrec, M. Molgg, A. Viscuso, R. Annunziata, A. Maurelli, P. Cappelletti, E. Ciantar, *2020 IEEE International Electron Devices Meeting* **2020**, pp. 24.2.1-24.2.4.

[10] A. Redaelli, A. Gandolfo, G. Samanni, E. Gomiero, E. Petroni, L. Scotti, A. Lippiello, P. Mattavelli, J. Jasse, D. Codegoni, A. Serafini, R. Ranica, C. Boccaccio, J. Sandrini, R. Berthelon, J.-C Grenier, O. Weber, D. Turgis, A. Valery, R. Gonella, *IEEE Journal of the Electron Devices Society* **2022**, 10, pp. 563-568.

[11] M. Baldo, O. Melnic, M. Scuderi, G. Nicotra, M. Borghi, E. Petroni, A. Motta, P. Zuliani, A. Redaelli, D. Ielmini, *2020 IEEE International Electron Devices Meeting* **2020**, pp. 13.3.1-13.3.4.

[12] M. Baldo, E. Petroni, L. Laurin, G. Samanni, O. Melinc, D. Ielmini, A. Redaelli, *2022 17th Conference on Ph. D Research in Microelectronics and Electronics (PRIME)* **2022**, pp. 145-148.

[13] M. Agati, M. Vallet, S. Joulié, D. Benoit, A. Claverie, *J. Mater. Chem. C* **2019**,7, pp. 8720-8729.

[14] E. Rahier, S. Ran, N. Ratel Ramond, S. Ma, L. Calmels, S. Saha, C. Mocuta, D. Benoit, Y. Le Friec, M. A. Luong, A. Claverie, *ACS Appl. Electron. Mater.* **2022**, 4, 6, pp. 2682–2688.

[15] L. Prazakova, E. Nolot, E. Martinez, D. Rouchon, F. Fillot, N. Bernier, R. Elizalde, M. Bernard, G. Navarro, *Materialia* **2022**, 21, 101345.

[16] V. Sousa, G. Navarro, in *Phase Change Memory* (Eds: A. Redaelli), Springer, **2018**, Ch.7, pp. 202-212.

[17] O. Abou El Kheir, M. Bernasconi, *Nanomaterials* **2021**, 11(9), 2382.

[18] S. Cecchi, I. Lopez Garcia, A.M. Mio, E. Zallo, O. Abou El Kheir, R. Calarco, M. Bernasconi, G. Nicotra, S.M.S. Privitera, *Nanomaterials* **2022**, 12(4), 631.

[19] E. Petroni, A. Serafini, D. Codegoni, P. Targa, L. Mariani, M. Scuderi, G. Nicotra, A. Redaelli, *Frontiers in Physics* **2022**, 10, 862954.

[20] E. Petroni, M. Patelmo, A. Serafini, D. Codegoni, L. Laurin, M. Baldo, A. Redaelli, https://doi.org/10.1002/pssr.202200458, **2023.**

[21] J. Aitchison, *The Statistical Analysis of Compositional Data*, Chapman and Hall, London, UK **1986**.

[22] C. C. Aggarwal, *Outlier Analysis*, Springer, New York, NY, USA **2013**.

[23] J. Sall, A. Lehman, M. Stephens, S. Loring, *JMP® Start Statistics: A Guide to Statistics and Data Analysis Using JMP®*, Sixth Edition, SAS Institute Inc., Cary, NC, USA **2017**.

[24] D. C. Montgomery and E. A. Peck, *Introduction to Linear Regression Analysis*, 2nd Edition, John Wiley & Sons Inc., Hoboken, NJ, USA **1992**.